Modeling of industrial-scale sorption enhanced gasification process: One-dimensional simulations for the operation of coupled reactor system

Ritvanen Jouni, Myöhänen Kari, Pitkäoja Antti, Hyppänen Timo

DOI: 10.1016/j.energy.2021.120387

Energy 226 (2021) 120387

Contents lists available at ScienceDirect

Energy

journal homepage: www.elsevier.com/locate/energy

Modeling of industrial-scale sorption enhanced gasification process: One-dimensional simulations for the operation of coupled reactor system

Jouni Ritvanen*, Kari Myöhänen, Antti Pitkäoja, Timo Hyppänen

Lappeenranta-Lahti University of Technology, LUT School of Energy Systems, P.O. Box 20, FI-53851, Lappeenranta, Finland

ARTICLE INFO

Article history:
Received 25 November 2020
Received in revised form
9 March 2021
Accepted 11 March 2021
Available online 23 March 2021

Keywords:
Sorption enhanced gasification
Biomass gasification
In-direct gasification
1D modelling
Dual fluidized bed
Coupled reactors

ABSTRACT

Sorption enhanced gasification (SEG) is a promising technology for producing gas derived from renewable feedstock to be used in biofuel synthesis processes. As a response to the growing need for renewable fuels, an SEG reactor design was developed for industrial-scale dimethyl ether (DME) production. A 100MW_{th} scale SEG reactor concept for wood pellets as a feedstock was created by a model-based approach. Thus, a 1D modeling tool for the coupled circulating fluidized beds was developed. The model was used to investigate the dual fluidized bed system's operation in the gasifier temperature range of 730–790°C. In this range, the optimal producer gas composition without external hydrogen for the downstream DME synthesis was achieved at gasifier temperature 730°C: 63 $\%_{vol,db}$ H_2, 11 $\%_{vol,db}$ CO, 13 $\%_{vol,db}$ CO_2. The model prediction was successfully compared against experimental data and modeling results from the literature. The developed 1D model enables the investigation of the composition and yield of the producer gas with different operating parameters, such as the part-load operation. This advanced capability can be used to develop new control strategies for the SEG system and investigate the impact of various operating parameters on the producer gas composition and yield.

1. Introduction

EU strategy for the transition to a low-carbon economy sets out a framework and mechanisms to address climate change. Greenhouse gas emissions from transportation account for almost a quarter of Europe's greenhouse gas emissions, and transportation is the primary source of air pollution in European cities [1]. The target of 14% renewable fuel usage in the transportation sector by 2030 has been set and, consequently, there is a pressing need to develop effective and cost-efficient ways to produce transportation fuels from renewable sources [2]. In recent decades, considerable research attention has been devoted to the study of conventional biomass gasification. However, in recent years, more advanced processes, such as dual fluidized bed gasifiers, have become the subject of increased research interest to produce tailored syngas for transportation biofuel production [3]. Sorbent enhanced gasification (SEG) is a dual fluidized bed technology that improves the syngas' quality compared to conventional gasification [4]. The SEG is an indirect steam gasification process operated at temperatures between 600 and 800°C, and the process is enhanced by limestone, which captures CO_2 from the gasification process. The removal of CO_2 from the gasifier enhances hydrogen production through the water-gas shift reaction. The schematic of the SEG process is illustrated in Fig. 1.

By the SEG operation, producer gas composition can be adjusted. The operating parameters affecting producer gas yield and composition are steam to carbon ratio, biomass feed rate to the combustor, solid inventories in the reactors, solids carrying capacity of CO_2, and solids circulation rate between the reactors. By these parameters, the reactors' temperature levels can be controlled, resulting in the target reaction environment. The gasifier temperature level is the most dominant controlling variable, which defines the limestone CO_2 capture yield by the carbonation reaction equilibrium.

The SEG and similar absorption enhanced reforming (i.e., AER) processes have been studied previously experimentally and in numerical simulations. The experimental investigations have mainly been carried out using pilot-scale test equipment from TU Wien [5,6] and the University of Stuttgart [7]. In these facilities, the

* Corresponding author.
E-mail address: jouni.ritvanen@lut.fi (J. Ritvanen).

https://doi.org/10.1016/j.energy.2021.120387

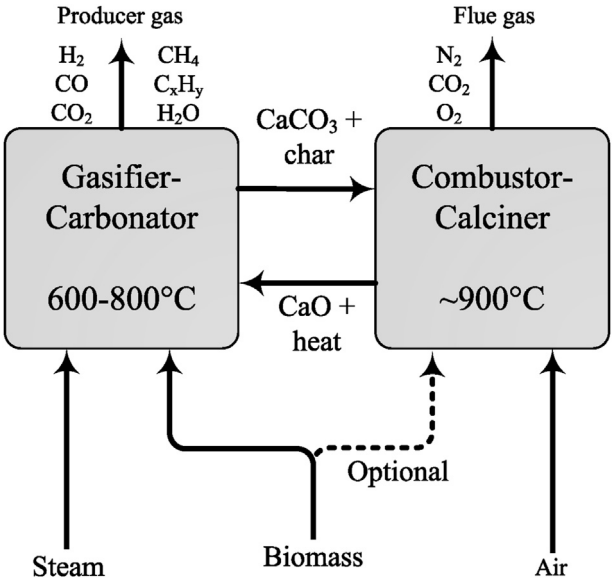

Fig. 1. Schematic of the SEG process.

gasifier is operated in bubbling fluidized bed (BFB) mode, and the combustor is operated in circulating fluidized bed (CFB) mode. Experimental results from these facilities are summarized in a review by Fuchs et al. [8]. The test results show the operation range of the SEG process in the temperature range of 600 – 850°C, which results in the corresponding H_2 gas concentrations 75 – 50%$_{db}$, CO gas concentrations 5 – 22%$_{db}$ and CO_2 gas concentrations 3 – 24%$_{db}$, respectively. The test results show the SEG process's controllability, enabling the flexible production of producer gas suitable for downstream processes. By adjusting the process, it is possible to maximize hydrogen production or, accordingly, to produce the desired ratio of gas components. Coupled SEG reactors have also been investigated numerically using simple lumped reaction equilibrium models [9,10], and kinetic reaction models [11,12] in a 1D simulation frame. These macroscopic models of coupled reactors have been implemented with the BFB gasifier and the CFB combustor on a pilot scale.

In this work, coupled SEG process is simulated on an industrial-scale using CFB technology in both reactors considering the reactors' hydrodynamics and using kinetic modeling for the reactions. These novel model approach and reactor combination have not been considered in the earlier studies. Here, CFB reactors have been selected, which are often more favorable and are used in larger industrial units due to their better mixing properties and smaller land area footprint. A model frame for the SEG process with CFB reactors was developed based on a semi-empirical 1D-approach. The model frame contains the gasification and the combustion reactors, coupled together to form a complete SEG process. Fundamental balance equations for mass and energy are implemented in the reactor model frame. This modeling approach involves coupled heat capacity flows from hydrodynamics that determines reactor temperatures. The model also considers solids' conversion degree between reactors obtained from a combination of solids inventories, reaction rates, and residence times. Transport phenomena and chemical reactions are modeled using empirical model equations validated with pilot-scale experiments and literature data. Reactor design with geometry and boundary condition data for the SEG system using biomass (i.e., wood pellets) as feedstock is proposed in this study. SEG model in a scale of 100MW$_{th}$ is used to estimate SEG operation in the gasifier temperature range of 730 – 790°C. The lower value of the temperature range is selected according to producer gas suitability for downstream Dimethyl ether (DME) synthesis with producer gas Module (M) of 2. The Module M is determined according to Eq. (1), using the ratio of the H_2, CO and CO_2 concentrations of the producer gas.

$$M = \frac{y_{H_2} - y_{CO_2}}{y_{CO} + y_{CO_2}} \quad (1)$$

The temperature range's upper value is based on the mixing of additional hydrogen from an external source with producer gas to make the producer gas suitable for DME synthesis. SEG system operation and performance values are investigated within the operation range of M = 2.17…0.7. This is the most interesting operation range for the DME synthesis. The model approach evaluates aspects of process operation and optimization that influence the process and plant design and form the basis for evaluating process performance and costs. One objective is to create a model frame that can investigate the process conditions outside of this study, such as different biomass feedstock.

2. One-dimensional SEG model

2.1. Reactor model frame

The overall 1D model frame can simulate a system of several interconnected reactors, each of which is discretized vertically into one-dimensional control volumes. The physical reactor scale is not limited: it can range from laboratory and pilot-scale to industrial scale. The effect of the scale is naturally considered in fundamental physical submodels or included in the empirical submodels and correlations. Fig. 2 presents the 1D-model for one CFB reactor including the cyclone-standpipe-loop seal system.

The overall model frame can contain several reactor models, which exchange solid material with each other. Time-dependent conservation equations for mass, energy, and gas and solid material fractions have written using the first-order difference method and the forward Euler method. The convective flows are differentiated with the upwind method, and the diffusion of energy is differentiated with the central difference method. These equations are solved in the Matlab Simulink environment using built-in ordinary differential equation (ODE) solvers. The reactor models are capable of using constant and variable time steps with ODE solvers. In this study, simulations are continued until the steady-state is reached for the SEG system.

The discretization scheme has three regions related to the chosen reactor geometry, namely straight bottom and freeboard sections, and a conical frustum part between these sections. The user-defined number of discretization elements with geometry data can be set for all regions independently. Elevation to exit channel defines the exit channel location, and the model collects and averages flow properties from discretized 1D elements located next to the exit channel. The gas phase's main boundary conditions include primary gas feed, and a user-defined number of secondary gas feeds with feed point elevation data. The fuel is numerically decomposed into char, ash, volatile, tar, and moisture fractions. In CFB conditions, volatile, tar, and moisture fractions are released in the reactor's bottom section, where larger fuel particles settle after the feeding. In the model's steady-state conditions, the rates of released components in the bottom section equal to the amount of components in the fuel feeding. Therefore, in the model, the total amount of volatile, tar, and moisture fractions in the fuel feed are released to the gas phase in the bottom section, which typically consists of 2–4 lowest elements of the reactor model. The

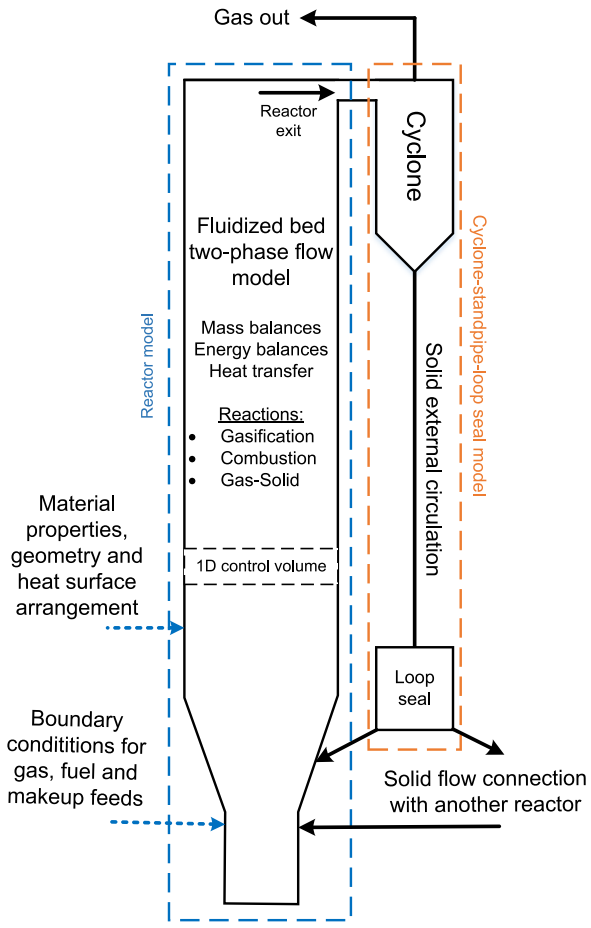

Fig. 2. Overview of the 1D model frame for the CFB reactor.

heterogeneous reactions connect gas-phase mass balance with solid-phase mass balance. Thirteen gas species (O_2, N_2, CO_2, H_2O, NH_3, H_2S, CO, CH_4, C_2H4, H_2, NO, SO_2 and tars) are solved in gas phase with heterogeneous and homogeneous reaction schemes. The solid phase is divided into char and primary solid material with separate reactor-level inventory balances. The primary solid's consists of four solid materials: CaO, $CaCO_3$, $CaSO_4$ and ash. The primary solid's main boundary conditions include a user-given solid inlet flow profile, fuel ash, and makeup flow sources. A separate solid purge can be used to control the primary solid inventory in the reactor. In connection with the material purge, char is removed at the discharge location in proportion to the materials' concentrations. Fuel ash source, makeup flow, and solid purge are located at the bottom of the reactor (i.e., in the first element). Char has the reactor-level mass inventory to which char from the fuel is added. Primary solid and char inventories are distributed to the reactor by the vertical density profiles. The solid-phase flow scheme includes wall layer flow (i.e., 1.5D-model) used in larger reactors to model horizontal and vertical mixing in the reactor. The mass balance of the char includes char combustion and gasification reactions. The Ca-containing materials are solved with the dominant reaction schemes for calcitic limestone. The ash is assumed inert. According to mass balances, gas and solids flow rates combined with local reactions determine the gas species' concentration profiles and solids material fraction profiles. The general form of the mass balance for material j and discretized element i is given in Eq. (2).

$$\frac{dm_{j,i}}{dt} = \sum_{in} q_{m,j,i} - \sum_{out} q_{m,j,i} + \sum_{reaction} r_{j,i}, \tag{2}$$

where $q_{m,j}$ represents the mass flow rate of material j and $r_{j,i}$ represents the change of mass due to chemical reactions. The energy balance scheme includes input and output streams of gas and solid, reaction heats, heat transfer to cooling surfaces, and energy dispersion between adjacent control volumes to model energy mixing. Heat transfer to cooling surfaces has three main options. Reactor configuration with refractory linings can be modeled with heat conduction through the wall. Also, a heat transfer to a plain reactor wall can be modeled. An internal plain wall heat surfaces can also be included in the model with location and heat surface area data. The general form of the energy balance for element i is given in Eq. (3).

$$\frac{dE_i}{dt} = \sum_{solid} q_{adv,i} + \sum_{gas} q_{adv,i} + \sum_{solid} q_{disp,i} + \sum q_{ht,i} + \sum q_{r,i}, \tag{3}$$

where q_{adv} is advection, q_{disp} is energy dispersion between adjacent elements, q_{ht} is the heat transfer to the cooling surfaces and q_r is reaction heat. The energy dispersion term represents the mixing of energy between adjacent control volumes, and it is written by applying the central difference method to Fick's law of diffusion.

A large number of continuous state variables are included in the model. The reactor's general state variables are total solid mass, total char mass, and total volatile and tar release rates. Also, state profiles with n_{tot} (i.e., the total number of 1D elements) variables for solid density, char density, the concentration of gas species, core temperature, wall layer temperature, wall layer solid density, and solid material fractions in core and wall layer are solved. Furthermore, two-dimensional state variables are included in the model for refractory lining temperatures. As a model input, amounts and compositions of primary and secondary gases, fuel, and solid makeup flow are given. The primary gas is inserted into the first control volume, and secondary gases can be inserted into any control volumes based on the secondary gas feed elevation. The solids input is divided to enter the selected control volumes according to design and exits the reactor from the control volumes located at the exit. Surface temperatures of heat surfaces are given as an input. The inputs are given as a time-vector to the Matlab Simulink solver. The solver requires the initial state values for each continuous variable, read from the state file.

2.2. Fuel decomposition

According to the fuel's proximate analysis, the fuel decomposition model divides the fuel into moisture, ash, volatiles, char, and tar. Elements C, N, O, H and S are divided between tar, char, and volatiles based on fuel analysis data. Submodels for char material fractions with tar composition are used to divide elements into volatile, tar, and char. For tar, C_7H_8 hydrocarbon is used as a model component to represent overall tar composition. The C_7H_8 hydrocarbon was selected to describe tars based on SEG test results [13] to represent the measured ratio of Carbon and Hydrogen and satisfy the elemental material balance. The fuel decomposition model generates reactive gas and solid fractions with theoretical reaction heats. This reaction heat is balanced with moisture latent heat and volatilization heat to obtain a measured lower heating value (LHV) of the fuel for the model.

In a standard laboratory analysis (DIN 51720), the sample's devolatilization temperature is 900°C. The actual process temperature inside the gasifier is below 800°C. A lower process

temperature is considered in the primary fuel decomposition, and temperature-dependent decomposition for volatiles, char, and tars is used instead of standard proximate data. For fuel moisture and amount of ash, a standard proximate data is used, shown with fuel's ultimate data in Table 1.

In the analysis, the volatile content was determined according to DIN 51720, but at temperatures 650…800°C. Within this range, char formation represents a process conditions of the SEG. With this data, the char fraction of the fuel was obtained in a function of a gasification temperature T_{gasif} in °C. An empirical correlation for char formation is given in Eq. (4).

$$x_{char,ds} = \max\left[-1.72\times10^{-4}T_{gasif} + 0.3037, 0.17\right], [\mathrm{kg_{char}}/\mathrm{kg_{ds}}] \quad (4)$$

The amount of the formed tars during the fuel decomposition is modeled by combining the measured tar yield from SEG experiments [13] and producer gas yield reported by Fuchs et al. [8]. Linear dependency for tar formation is assumed in the investigated temperature range. Empirical correlation for tar formation is presented in Eq. (5).

$$x_{tar,ds} = -2.0\times10^{-5}T_{gasif} + 2.92\times10^{-2}, [\mathrm{kg_{tar}}/\mathrm{kg_{ds}}] \quad (5)$$

The volatile fraction of the fuel is calculated from the following Eg. 6.

$$x_{vol,ds} = 1 - x_{char,ds} - x_{tar,ds} - x_{ash,ds} \quad (6)$$

In the fuel decomposition model, empirical correlations by Neves et al. [14] are used for Carbon (Eq. (7)) and Hydrogen (Eq. (8)) fractions in char, and empirical correlations by Myöhänen [15] are used for fractions of Nitrogen (Eq. (9)) and Sulphur (Eq. (10)) in char. Correlations for C and H composition of the char are according to Neves et al. [14]:

$$x_{char,\mathrm{C}} = 0.93 - 0.92\exp\left(-4.2\times10^{-3}T_{gasif}\right) \quad (7)$$

$$x_{char,\mathrm{H}} = -4.1\times10^{-3} + 0.1\exp\left(-2.4\times10^{-3}T_{gasif}\right). \quad (8)$$

N and S elements are assumed to follow correlations by Myöhänen [15]:

$$x_{char,\mathrm{N}} = 8.8\times10^{-2}x_{F,\mathrm{N}}x_{char,daf}^{0.6}\left(\frac{x_{F,\mathrm{N}}}{x_{F,\mathrm{C}}}\right)^{-0.6} \quad (9)$$

$$x_{char,\mathrm{S}} = 0.14x_{F,\mathrm{S}}x_{char,daf}^{0.2}\left(\frac{x_{F,\mathrm{H}}}{x_{F,\mathrm{C}}}\right)^{-0.6}, \quad (10)$$

where $x_{F,i}$ is fraction an element of char's parent fuel according to the ultimate analysis. The oxygen fraction of the char is calculated from the Eq. (11).

Table 1
Chemical composition of wood pellets.

Fuel	Wood pellets
C [wt-%,daf]	51.82
H [wt-%,daf]	6.15
N [wt-%,daf]	0.2
S [wt-%,daf]	0.02
O [wt-%,daf]	41.81
Moisture [wt-%,ar]	15.0
Ash [wt-%,ds]	1.15
LHV [MJ/kg,ar]	16.37

$$x_{char,\mathrm{O}} = 1 - x_{char,\mathrm{C}} - x_{char,\mathrm{H}} - x_{char,\mathrm{N}} - x_{char,\mathrm{S}} \quad (11)$$

The volatiles' elemental composition is calculated from the balance (Eq. (12)) using the ultimate analysis data and compositions of char and tar.

$$x_{vol,i} = x_{F,i} - x_{char,daf}x_{char,i} - x_{tar,daf}\frac{M_{tar,i}}{M_{tar}} \quad (12)$$

Based on stoichiometry NH_3, H_2S, CO, CO_2, CH_4, C_2H_4 and H_2 gases are formed from volatilized elements. The stoichiometric composition can be adjusted with model parameters γ_1 and γ_2:

$$\gamma_1 = \frac{n_{\mathrm{CO}}}{n_{\mathrm{CO}} + n_{\mathrm{CO_2}}} \quad (13)$$

$$\gamma_2 = \frac{n_{\mathrm{CH_4,C}}}{n_{\mathrm{CH_4,C}} + n_{\mathrm{C_2H_4,C}}} \quad (14)$$

For the formation of the volatile species, following procedure is applied:

1. Volatile S and N are used to form H_2S and NH_3, respectively.
2. Volatile O is used to form CO and CO_2 in a ratio of γ_1, defined in Eq. (13).
3. Leftover Carbon after step 2. is used to form hydrocarbons CH_4 and C_2H_4 in a ratio of γ_2, defined in Eq. (14).
4. Leftover Hydrogen after steps 1. and 3. is used to form H_2

Measured Hydrocarbon concentrations from SEG experiments [13] and producer gas yield reported by Fuchs et al. [8] were used to develop empirical correlations for γ_i, which are presented in Eqs. (15) and (16).

$$\gamma_1 = 1.626\times10^{-4}T_{gasif} + 0.703 \quad (15)$$

$$\gamma_2 = -4.38\times10^{-8}T_{gasif}^2 + 8.142\times10^{-5}T_{gasif} + 0.612 \quad (16)$$

2.3. Reactions

In this study, homogeneous gas reactions and heterogeneous reactions for limestone and char are considered. Limestone and gasification reactions are summarized in Table 2.

In oxidation conditions, a combustion reaction is applied for char with reaction rate by Basu [25]. The different combustible gaseous species produced from fuel decomposition, tar release, char combustion, and gasification will react in the presence of oxygen. The kinetic reaction rates of homogeneous combustion reactions are determined with the generic correlation given in Eq. (17).

$$r_{gas} = A_0T^{a_1}C_{gas}^{a_2}C_{\mathrm{O_2}}^{a_3}C_{\mathrm{H_2O}}^{a_4}\exp\left(\frac{-T_e}{T}\right), \left[\mathrm{mol}\,/\left(\mathrm{m^3 s}\right)\right] \quad (17)$$

The modeled homogeneous reaction equations with reaction rate parameters are given in Table 3.

2.4. Solid hydrodynamics

The vertical distribution of solid material in the reactor is solved by dividing the total solid mass into the reactor with a semi-empirical correlation presented in Eq. (18) by Johnsson and Leckner [32].

Table 2
Limestone and gasification reactions. Heterogeneous reactions in $R_i = [\mathrm{kg}/(\mathrm{m^3 s})]$ and homogeneous reactions in $r_i = [\mathrm{mol}/(\mathrm{m^3 s})]$.

Reaction	Equation	ΔH_{298K} [kJ/mol]	Ref.
Calcination	$CaCO_3(s) \rightarrow CaO(s) + CO_2(g)$	178.2	
	$R_{calc} = k_{calc}\rho_s W_{CaCO_3}^{0.67}(C_{CO_2,eq} - C_{CO_2})$		[16]
	$k_{calc} = 2057\exp\left(-\frac{112400}{RT}\right)$		[17]
	$C_{CO_2,eq} = \frac{4.137\times10^{12}}{RT}\exp\left(-\frac{20474}{T}\right)$		[18]
Carbonation	$CaO(s) + CO_2(g) \rightarrow CaCO_3(s)$	−178.2	
	$R_{carb} = k_{carb}\rho_s(W_{CaCO_3,max} - W_{CaCO_3})^{0.67}(C_{CO_2} - C_{CO_2,eq})$		[19]
	$k_{carb} = 0.3429 f_{carb}\exp\left(-\frac{2309}{T}\right)$		[19]
	$f_{carb} = 0.9$		
Sulphation	$CaO(s) + SO_2(g) + 0.5O_2(g) \rightarrow CaSO_4(s)$	−502.3	
	$R_{sulp} = k_{sulp}\rho_s W_{CaO} W_{SO_2} W_{O_2}$		[20]
	$k_{sulp} = 4.0(-3.843T + 5640)\exp\left(-\frac{8810}{T}\right)$		[20]
Direct Sulphation	$CaCO_3(s) + SO_2(g) + 0.5O_2(g) \rightarrow CaSO_4(s) + CO_2$	−324.1	
	$R_{dirs} = k_{dirs}\rho_s W_{CaCO_3} C_{SO_2}^{0.9} C_{CO_2}^{-0.75} C_{O_2}^{0.001}$		[15]
	$k_{dirs} = 0.01\exp\left(-\frac{3031}{T}\right) A_{m,CaCO_3} M_{CaCO_3}$		[15]
	$A_{m,CaCO_3} = 300\ [\mathrm{m^2/kg}]$		[15]
Desulphation	$CaSO_4(s) + CO(g) \rightarrow CaO(s) + SO_2 + CO_2$	219.3	
	$R_{desu} = k_{desu}\rho_s W_{CaSO_4} C_{CO}$		[15]
	$k_{desu} = 0.005\exp\left(-\frac{10000}{T}\right) A_{m,CaSO_4} M_{CaSO_4}$		[15]
	$A_{m,CaSO_4} = 100\ [\mathrm{m^2/kg}]$		[15]
Boudouard	$C(s) + CO_2(g) \rightarrow 2CO(g)$	172.4	
	$R_{boud} = k_{boud}\rho_{char} W_{char,C}$		[21]
	$k_{boud} = 2.11\times10^{7}\exp\left(-\frac{219000}{RT}\right) p_{CO_2}^{0.36}[\mathrm{bar}]$		[21]
Water-gas	$C(s) + H_2O(g) \rightarrow CO(g) + H_2(g)$	131.3	
	$R_{wg} = k_{wg}\rho_{char} W_{char,C}$		[22]
	$k_{wg} = 1.23\times10^{7}\exp\left(-\frac{198000}{RT}\right) p_{H_2O}^{0.75}[\mathrm{atm}]$		[22]
Methanation	$C(s) + 2H_2(g) \rightarrow CH_4(g)$	−74.6	
	$R_{mf} = k_{mf}\rho_{char} W_{char,C}$		[23]
	$k_{mf} = 16.4\exp\left(-\frac{94800}{RT}\right) p_{H_2}^{0.93}[\mathrm{MPa}]$		[23]
Water-gas-Shift	$CO(g) + H_2O(g) \rightarrow H_2(g) + CO_2(g)$	−41.1	
	$r_{wgs} = k_{wgs}(C_{CO}C_{H_2O} - C_{CO_2}C_{H_2}/K_{wgs}) f_{wgs}$		[24]
	$k_{wgs} = 2.78\exp\left(-\frac{12560}{RT}\right)$		[24]
	$K_{wgs} = 0.0265\exp\left(\frac{3956}{T}\right)$		[23]
	$f_{wgs} = 0.075$		

Table 3
Reaction rate parameters for homogeneous combustion reactions.

Reaction equation	ΔH_{298K} [kJ/mol]	gas	A_0	a_1	a_2	a_3	a_4	T_e	Ref.
$C_2H_4 + 3O_2 \rightarrow 2CO + 2H_2$	−1323.2	C_2H_4	6.3×10^{7}	0.0	0.1	1.65	0.0	15106	[26]
$CH_4 + 0.5O_2 \rightarrow CO + 2H_2$	−802.6	CH_4	3.6×10^{11}	−1.0	1.0	1.0	0.0	15700	[27]
$H_2S + 1.5O_2 \rightarrow SO_2 + H_2O$	−518.0	H_2S	2.8×10^{9}	0.0	1.074	1.084	0.0	18956	[28]
$CO + 0.5O_2 \rightarrow CO_2$	−283.0	CO	7.3×10^{14}	0.0	1.0	0.25	0.5	34745	[29]
$H_2 + 0.5O_2 \rightarrow H_2O$	−241.8	H_2	1.6×10^{9}	−1.5	1.5	1.0	0.0	3430	[30]
$C_7H_8 + 3.5O_2 \rightarrow 7CO + 4H_2$	−3772.0	C_7H_8	5.0×10^{6}	0.0	0.1	1.85	0.0	15106	[26]
$NH_3 + 1.25O_2 \rightarrow NO + 1.5H_2O$	−902.1	NH_3	1.9×10^{9}	0.0	0.86	1.04	0.0	19655	[31]

$$\rho_s(h) = [\rho_b - \rho_e\exp(Kh_e)]\exp(-ah) + \rho_e\exp[K(h_e - h)], \quad (18)$$

where ρ_b is the bottom density, ρ_e is the exit density at the elevation h_e, a represents the splash zone decay coefficient and K represents the transport zone decay coefficient. Empirical correlations for decay coefficients a and K [32] are given in Eqs. (19) and (20), respectively.

$$a = \frac{4u_t}{u_{grid}} \quad (19)$$

$$K = \frac{0.23}{u - u_t}, \quad (20)$$

where u is the superficial gas velocity at the transport zone, u_t is the terminal velocity of the particle, and u_{grid} is the superficial gas

velocity at the grid. Solid density at the exit is calculated with a linear function according to Eq. (21).

$$\rho_e = \rho_{s,av}\frac{u - u_t}{u_{pn} - u_t} \tag{21}$$

where $\rho_{s,av}$ is the average solid density in the reactor, and u_{pn} represents the corresponding transport velocity of the gas. The solid mass flow rate out from the reactor is approximated with a semi-empirical correlation given in Eq. (22) by Ylätalo [33].

$$q_{m,s,e} = 0.85 u A_e \rho_e^{0.8} \tag{22}$$

3. Simulation setup for coupled SEG reactor system

The SEG configuration was built by coupling two CFB reactors together. The reactor coupling was done by connecting solid streams from the reactor to another. The coupled reactor system is illustrated in Fig. 3. Both reactors have a circular cross-section, straight bottom and freeboard sections, and a conical frustum between these sections. On design basis, 100 MW_{th} fuel power and superficial gas velocity of 5 m/s in both reactor were used. Steam to Carbon ratio (S/C) on a molar basis was fixed to 1.5.

The dimensions of the reactors and material properties for char and limestone are given in Table 4.

Ten operation points were investigated, covering the SEG operation range for producer gas Module from 2 to 0.7. Definition for producer gas module M is given in the Eq. (1). The SEG operation was investigated with a temperature limit of 950°C for the combustor. A constant heat loss of 20.0 kW/m was applied to model a heat loss of the reactors. Cyclone efficiencies after the reactors were set for limestone, ash, and char separately with values of 0.999, 0.995, and 0.99, respectively. The maximum carbonation degree for the limestone was set to 0.25 as mass-based. Boundary conditions for the operation points are presented in Table 5.

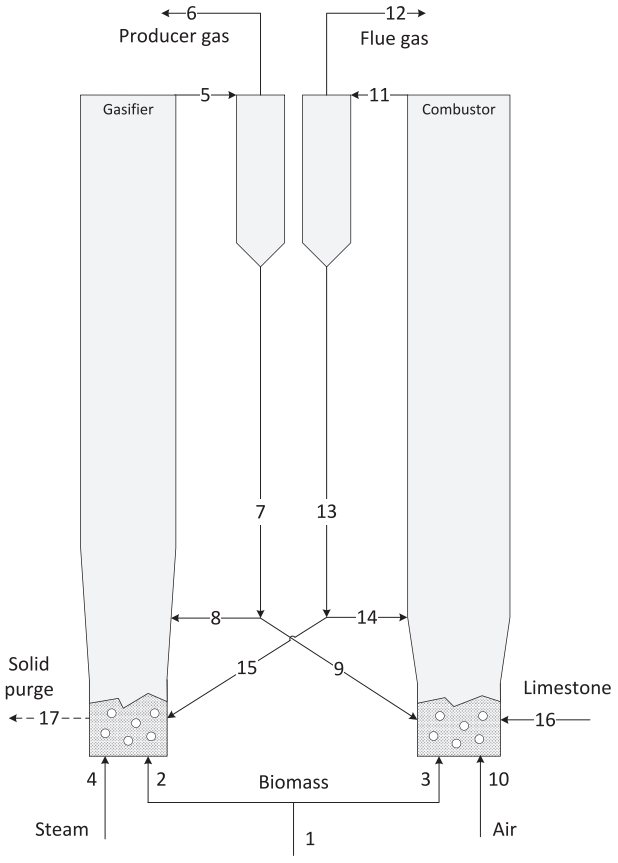

Fig. 3. SEG configuration with connection streams.

Table 4
Dimensions of the SEG reactors and solid material properties.

	Gasifier	Combustor
Height of the bottom section, m	2.3	2.2
Height of the frustum section, m	4.00	2.00
Height of the reactor, m	20.00	20.00
Diameter of the grid, m	2.35	2.51
Diameter of the freeboard, m	2.88	3.09
Number of nodes in bottom section	5	5
Number of nodes in frustum section	8	4
Number of nodes in freeboard section	27	31
Elevation of secondary gas feed, m	1.0	1.0
Elevation of tertiary gas feed, m	2.0	2.0
Elevation of input solid flow channel, m	0–0.9	0–0.9
Elevation of external circulation channel, m	0–0.9	0–0.9
Solid exit to another reactor, m	18.00	18.00
Limestone particle diameter, μm	150	150
Limestone particle density, kg/m^3	3000	3000
Limestone specific heat, J/kgK	1050	1050
Char particle diameter, μm	300	300
Char particle density, kg/m^3	550	550
Wood pellet particle diameter, mm	6	6

4. Results and discussion

1D simulation results for the industrial-scale SEG system is shown in ten operating points (OP) covering an operational range for producer gas M value from 2.17 (OP1) to 0.7 (OP10). The Module range is achieved within the gasifier temperature range of 730°C (OP1) to 786°C (OP10). 1D simulation results for producer gas yield and composition are compared against experimental results [13] and an SEG review study by Fuchs et al. [8]. Simulated temperature range and solid's circulation rates in the SEG system are illustrated in Fig. 4.

The temperature range is achieved by changing the fuel feed ratio to the combustor and controlling the temperature difference between the reactors with system hydrodynamics. Increasing the solid's inventory or gas velocity will lead to a higher solid's circulation rate and a smaller temperature difference between the reactors. In the SEG system, the gasifier's temperature is the most dominant factor in defining SEG performance. The gasifier temperature will determine the producer gas yield and composition by carbonation and water-gas shift reactions. Simulated producer gas yield is presented in Fig. 5, which is consistent with the SEG range by review work of Fuchs et al. [8].

Simulation results for the main produced gas concentrations and corresponding producer gas module M are presented in Fig. 6. All the main gas concentrations are consistent with the SEG range by review work of Fuchs et al. [8] and with experimental data for wood pellets [13] with steam to carbon ratio of 1.5. Estimation for producer gas module *M* was achieved within the investigated temperature range.

In the current simulation approach, hydrocarbons are considered only in gaseous form and are divided into three groups: 1) methane CH_4 2) light hydrocarbons C_2H_4 and 3) heavy hydrocarbons (i.e., tars) C_7H_8. Simulation results for hydrocarbons in producer gas are illustrated in Fig. 7. Amounts of the hydrocarbons in the producer gas are consistent with the SEG range by review work of [8] and with experimental data [13].

Table 5
Boundary conditions for the SEG simulations. Stream numbers (S#) refer to numbering in Fig. 3.

	S#	OP1	OP2	OP3	OP4	OP5	OP6	OP7	OP8	OP9	OP10
Fuel feed, kg/s	1	6.644									
Fuel feed, MW	1	108.8									
Fuel to combustor, %	3	1	2	3	4	5	6	6	6	6	6
S/C, mol/mol	4/2	1.5									
CO_2 feed[a], kg/s	4	0.2									
CO_2 feed[a], °C	4	25									
Steam, °C	4	200	200	200	200	200	200	300	400	400	400
O_2, v − $\%_{db}$	12	3.0	3.0	3.0	3.0	3.0	3.0	3.5	4.7	4.7	4.7
Air, °C	10	250									
$CaCO_3$, kg/s	16	0.5									
$CaCO_3$, °C	16	20									
Grid over pressure[b], Pa	4,10	4500	4500	4500	4500	4500	4500	4500	4750	5000	5250
Exit pressure, kPa	6,12	143									
Solid purge, kg/s	17	0.163	0.156	0.150	0.144	0.138	0.131	0.122	0.097	0.088	0.080

[a] Sealing gas.
[b] Pressure difference caused by the solid material in the reactor.

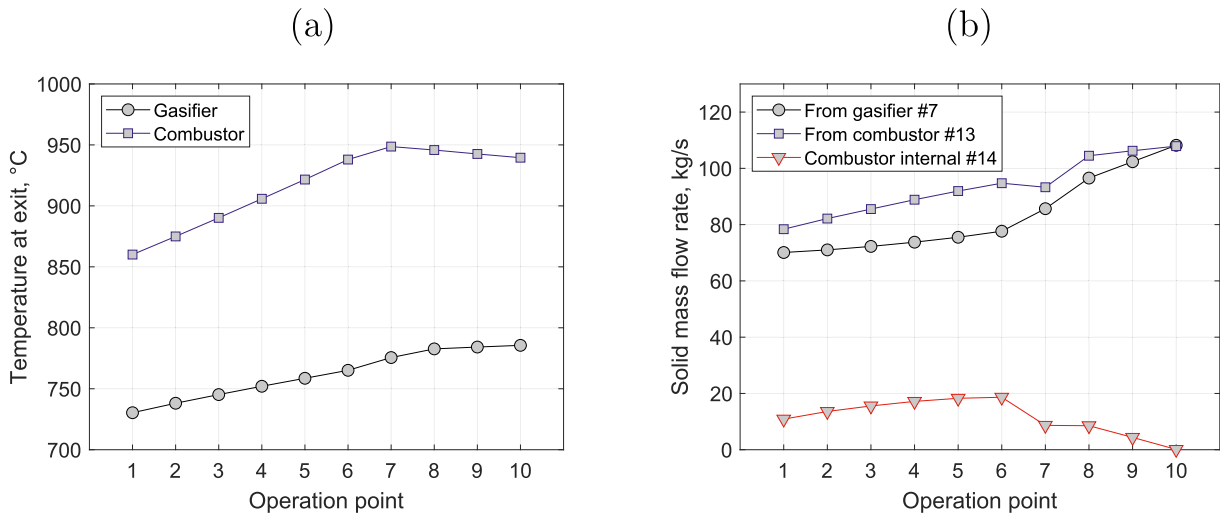

Fig. 4. Simulated temperatures (a) and mass flow rates (b) from the gasifier and the combustor.

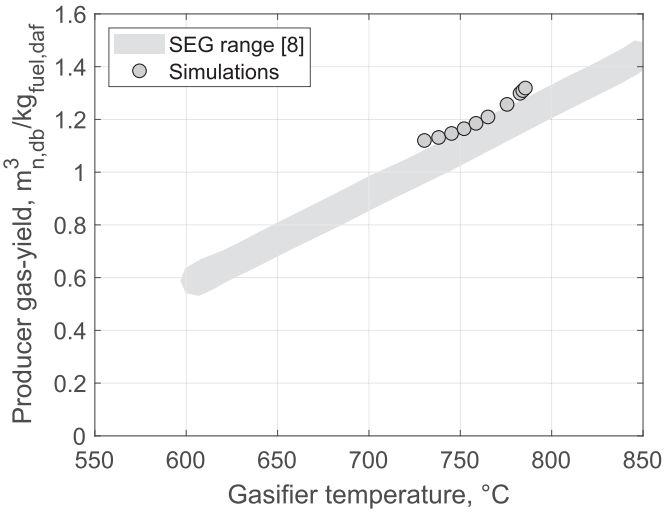

Fig. 5. Producer gas yields a function of gasifier peak temperature.

Overall performance indicators for the SEG system can be derived using a producer gas yield and composition data. Cold gas efficiency (CGE) values have been derived for the producer gas considering different gas species. The general form for CGE in lower heating value basis is given in Eq. (23).

$$\mathrm{CGE} = \frac{q_{m,pg} \sum x_i \mathrm{LHV}_i}{P_{fuel}} \tag{23}$$

where $q_{m,pg}$ is the producer mass flow rate, x_i is mass fraction of gas species i with lower heating value LHV_i, and P_{fuel} is fuel power fed to the gasifier in LHV basis. Simulated CGE values with and without methane and light hydrocarbons are illustrated in Fig. 8.

In the CGE calculations, tars are excluded. Maximum CGE = 75.4% with methane and light hydrocarbons is obtained at OP10 in the gasifier temperature of 786°C. Throughout the investigated temperature range, the methane and light hydrocarbon part in the CGE are approximately 29%-units. Methane and light hydrocarbons should be exploited in downstream processes to capture fuel power most efficiently. Carbon conversion (CC) into the producer gas, tar, char, and $CaCO_3$ is investigated and determined by the Eq. (24), considering the effect of CO_2 sealing gas.

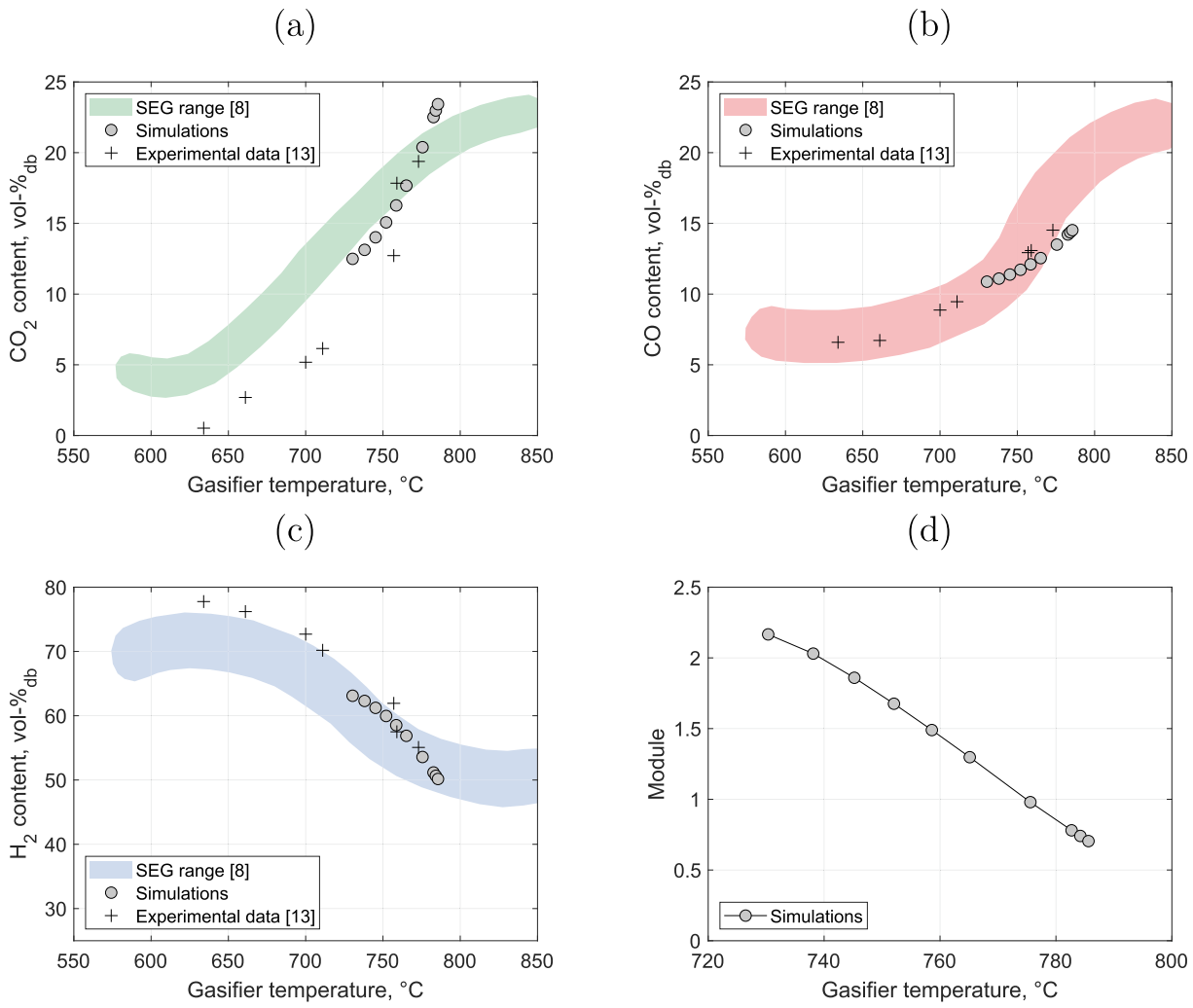

Fig. 6. Concentrations of main producer gas species (a) CO_2, (b) CO, (c) H_2 and corresponding module M in (d).

$$CC_i = \frac{q_{m,C,i}}{q_{m,C,fuel} + q_{m,C,CO_2}} \tag{24}$$

Carbon conversion and carbon transport to combustor are presented in Fig. 9.

The carbon conversion to char is slightly decreasing as the temperature is increased. This is mainly caused by the fuel decomposition model that forms less char in higher temperatures, and there is a slight increase in char gasification on the elevated temperatures. Carbon conversion to Calcium material is reduced significantly on the elevated temperatures shifting the carbon conversion towards producer gas. On the elevated temperatures, gasifier operation approaches the carbonation equilibrium reducing the CO_2 capture. The carbon transport from the gasifier to the combustor is compared with the model prediction by Fuchs et al. [8]. Simulation results are consistent with the model prediction by Fuchs et al. [8].

Carbonation and water-gas shift reactions are the most dominant SEG reactions, and these reactions mainly define the overall system performance. For these reactions, reaction rate definitions according to Table 2 are used. As a result of reaction kinetics in local system conditions, both reactions approach the thermodynamic equilibrium as operating temperature increases. The deviation from the equilibrium is determined by the expression given in Eq. (25).

$$p\delta_{eq} = \log_{10}\left[\frac{\prod_i p_i^{\nu_i}}{K_p(T)}\right] \tag{25}$$

The deviation from the equilibrium for the water-gas shift and the carbonation reactions are shown in Fig. 10.

In addition to the overall SEG results, the model provides 1D profile results for the reactors. Temperature profiles along the reactor height are presented in Fig. 11 for OP1 and OP10. Almost uniform temperature is predicted for both reactors with respect to the reactor height in the investigated operation range. The maximum of 50 °C temperature difference was predicted inside the reactors.

Carbonation, calcination, and water-gas-shift reaction are the most dominant SEG reactions to determine the local gas concentrations inside the reactors. Reaction rates for these reactions are illustrated in Fig. 12, at OP1 and OP10.

At OP1, the gasifier is entirely on the carbonation side, and the combustor is fully on the calcination side. At OP10, the bottom part of the gasifier is on the calcination side. Above 5 m, carbonation occurs until the top of the gasifier. The actual carbonation rate at OP10 is smaller compared to OP1, resulting smaller amount of $CaCO_3$ to be transferred to the combustor. At OP10, $CaCO_3$ fed to the reactor is fully calcined already at the bottom part of the combustor.

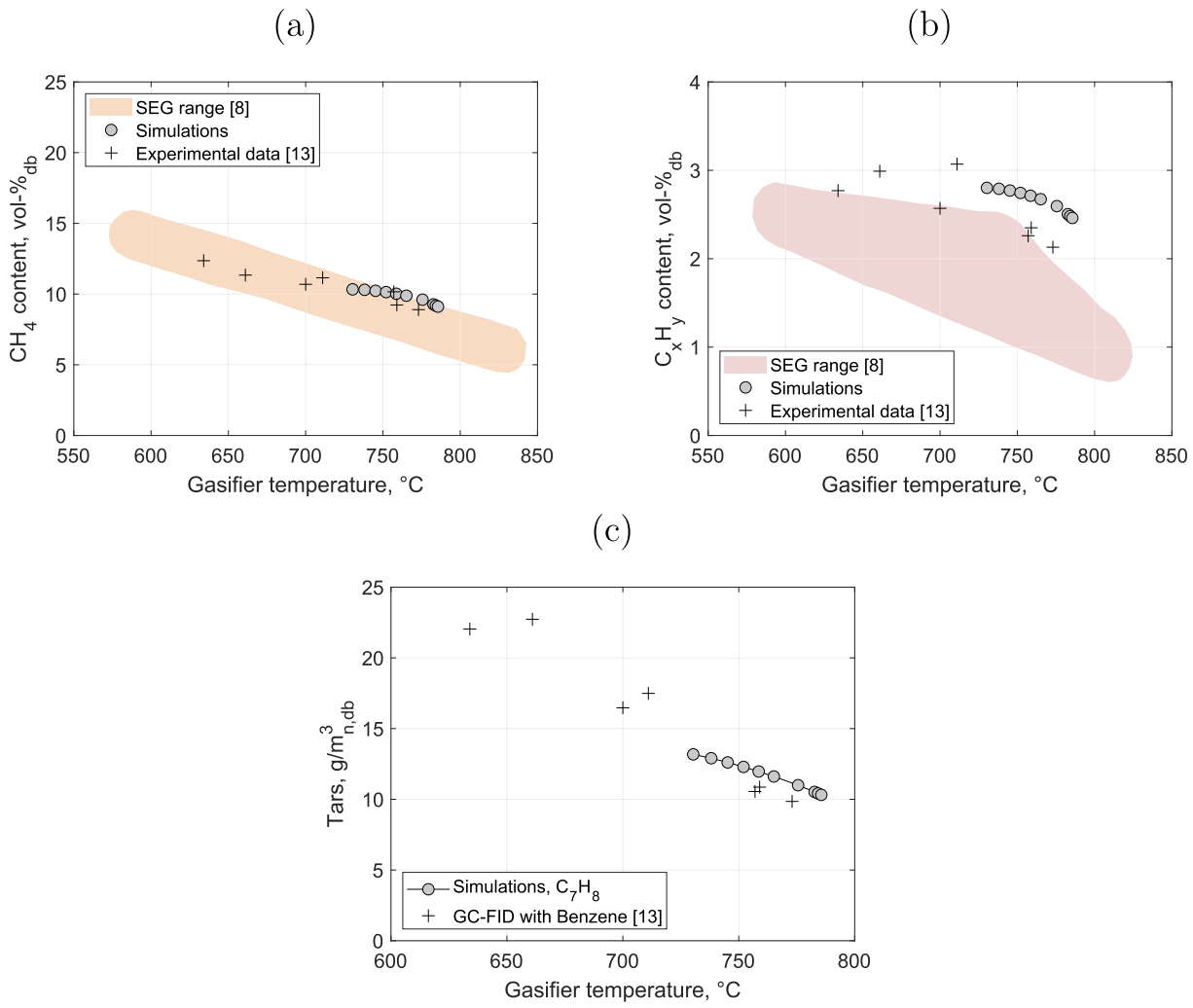

Fig. 7. Concentrations of hydrocarbons in producer gas. (a) methane CH_4, (b) light hydrocarbons C_xH_y and (c) tars C_7H_8.

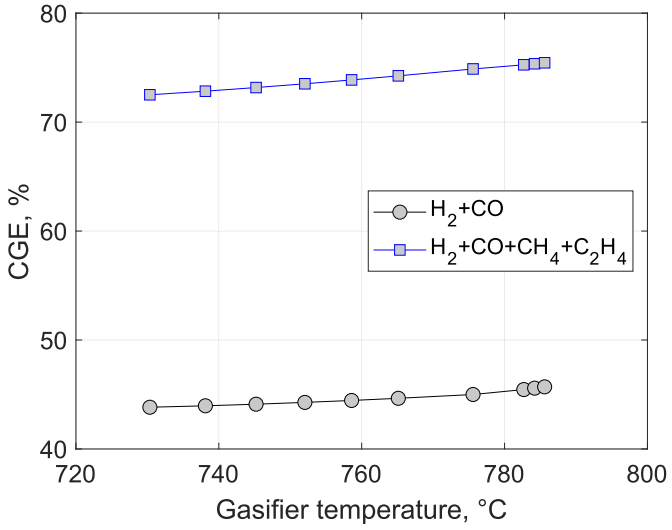

Fig. 8. Cold gas efficiencies (CGE) in a function of gasifier temperature. Simulation data with and without methane and light hydrocarbons.

In both operating points, water-gas shift reaction rate profiles are on a similar magnitude. A shift of the carbonation-calcination reaction direction at OP10 is illustrated in Fig. 13, where the local CO_2 concentration is plotted against local temperature that crosses the reaction equilibrium curve.

At OP1, combustor temperature is closer to the carbonation equilibrium resulting in slow calcination and partially calcined limestone material transfer to the gasifier. Increasing the combustor temperature at OP1 would increase the calcination rate leading to the fully calcined material output.

Simulated conversion degree profiles for $CaCO_3$ are presented in Fig. 14 for OP1 and OP10.

Minimal $CaCO_3$ content at the combustor bottom is observed at OP10. This is due to the low CO_2 capture on the gasifier side, leading to a low $CaCO_3$ concentration in the solids flow, as well as the relatively high combustor temperature. The low $CaCO_3$ concentration in the solids input stream keeps the $CaCO_3$ level very low on the combustor side. The high temperature of the combustor accelerates the calcination reaction, leading to the disappearance of the $CaCO_3$ fraction above the lower reaction zone. At OP1, about 1 m-% of $CaCO_3$ is estimated at combustor exit. On the gasifier side, small $CaCO_3$ content is observed at OP10 due to operation near the carbonation equilibrium. Maximum $CaCO_3$ conversion is observed at OP1 in the gasifier's exit with a value of 11 m-%. That is much

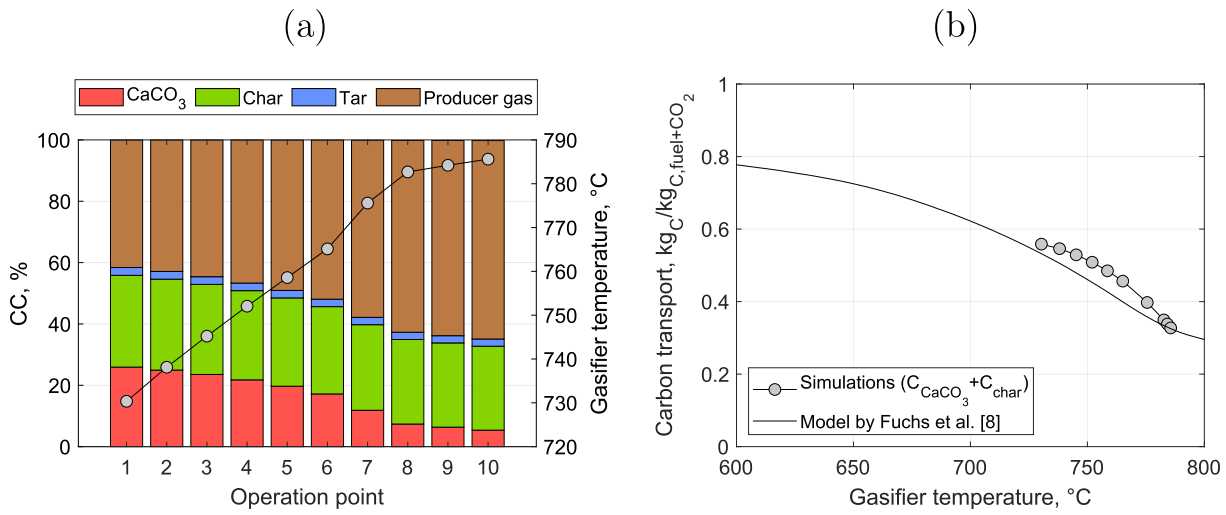

Fig. 9. (a) Carbon conversion to produced gas, tar, char and $CaCO_3$. Gasifier temperature presented with circles. (b) Carbon transport to combustor with char and $CaCO_3$.

smaller compared to the maximum $CaCO_3$ conversion degree of 25 m-%, set for the limestone material. A negligible amount of $CaSO_4$ was observed within the lime.

As a result of the reaction scheme connected with mass and energy balances, gas concentration profiles are obtained. The gas concentration profiles for the main gas species and both reactors are illustrated in Fig. 15.

In operation points OP1 and OP10, the effect of water-gas shift reaction can be observed. The water-gas shift reaction will reduce the CO and H_2O contents along with the reactor height. At the same time, H_2 and CO_2 contents are increasing. At OP1, H_2 content is increasing with a higher rate than CO_2. The formed CO_2 by the water-gas shift is captured and reduced by the carbonation reaction. At OP10, reduced CO_2 content at the combustor side is observed due to reduced CO_2 capture on the gasifier side. Gas concentrations on the gasifier side start to remain constant after 15 m and on the combustor side after 10 m of height.

The water-gas shift reaction balance profile is determined by using the gas concentration profiles of the gasifier. The water-gas shift reaction balance values in a function of corresponding local temperature are presented in Fig. 16 with the theoretical reaction equilibrium.

The water-gas shift reaction approaches the equilibrium but will not reach it. The water-gas shift reaction balance values for the gasifier output are shown in Fig. 10 expressed as a logarithmic distance from the equilibrium.

5. Conclusions

In this work, sorption enhanced biomass gasification on an industrial scale was studied. A 1D modeling tool for coupled reactors was used to design and investigate the SEG process on a $100MW_{th}$ scale. Based on the simulations, it was possible to demonstrate the wide operating range of the SEG process, where it is possible to produce producer gas with different compositions suitable for downstream biofuel syntheses. The optimal producer gas composition without external hydrogen for the downstream DME synthesis was achieved at gasifier temperature 730°C: 63 $\%_{vol,db}$ H_2, 11 $\%_{vol,db}$ CO, 13 $\%_{vol,db}$ CO_2, corresponding Module value of 2.1. The modeling method used took into account the hydrodynamic solids profiles and flow rates between the reactors. The thermal capacity

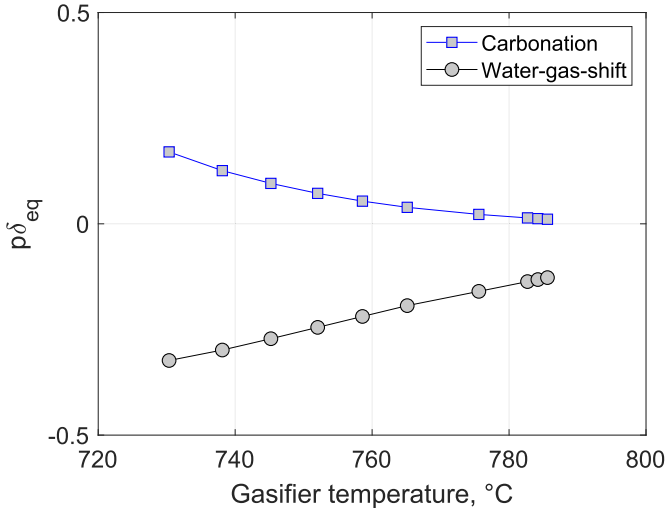

Fig. 10. Deviation of the equilibrium for carbonation and water-gas shift reactions.

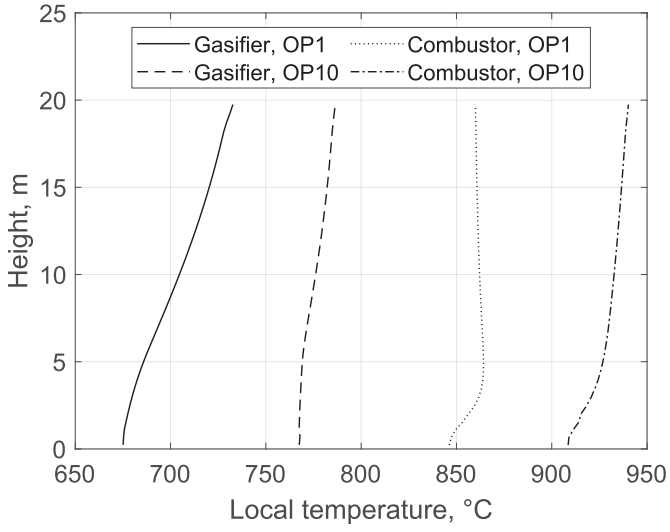

Fig. 11. OP1 and OP10 temperature profiles for both reactors along with the reactor height.

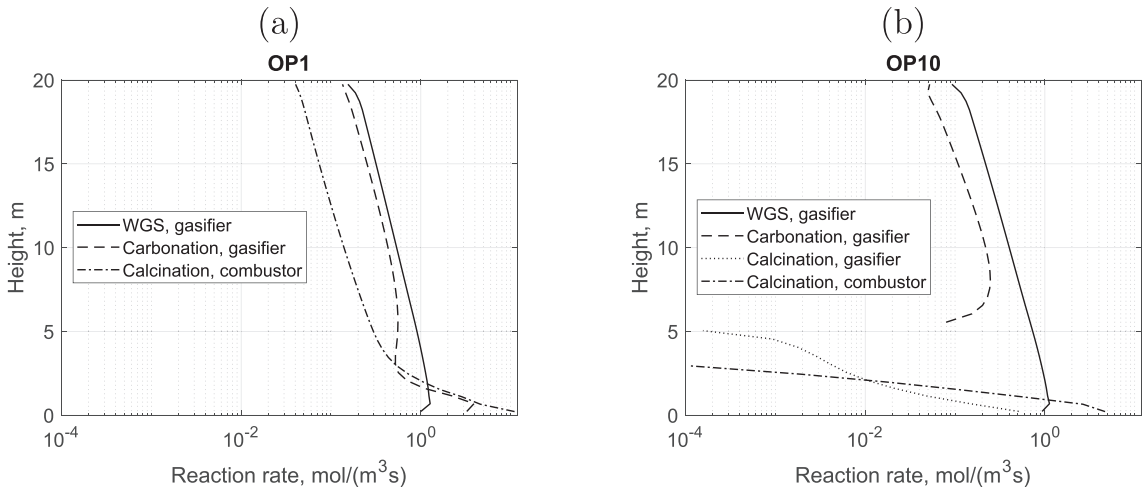

Fig. 12. Reaction rates for carbonation, calcination, and water-gas-shift along the reactor height. (a) OP1 and (b) OP10.

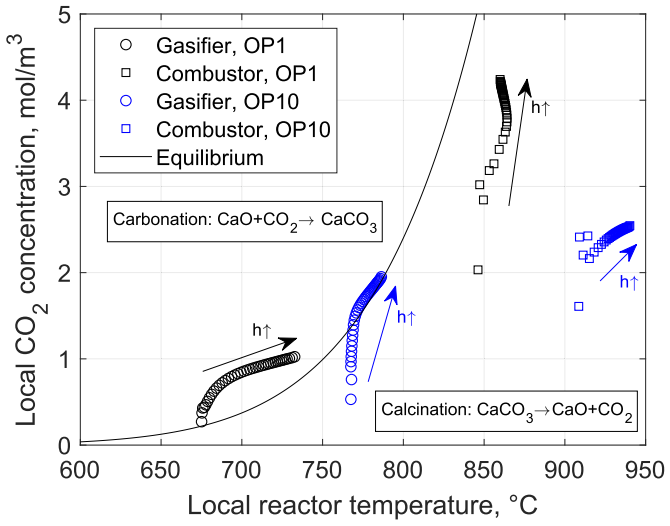

Fig. 13. Local CO_2 concentration in a function of local temperature with carbonation-calcination reaction equilibrium. Arrows show the direction of the reactor's vertical axes.

flows according to the solids flow rates were taken into account in the connected reactors' energy balances, giving an accurate physical description of the reactor temperature levels. Also, the flow rates of solids, including their conversion degrees, provided a sound basis for considering heterogeneous reactions in reactors with sufficient accuracy. Unlike before, the modeling used a temperature-dependent fuel decomposition model, which gave a more detailed description of the fuel's behavior under the conditions of the reactors. This was able to guarantee more accurate source terms for the reaction descriptions, and ultimately a reliable prediction of the yield and composition of the product gas was achieved. This also included a forecast for the yields of light and heavy hydrocarbons to obtain more accurate predictions for the elemental distribution of producer gas. The simulation results obtained correspond to the results presented in the literature for a similar type of process. The work was also able to demonstrate the suitability of CFB-CFB for SEG processes using a simulation model. In the future, this investigation can be extended to part load cases where the total fuel feed to the SEG process is changed. In this way, it is possible to consider lower and higher gasifier temperatures, whereby the yield and composition of the product gas can be controlled over a broader range. Concerning the physical sub-

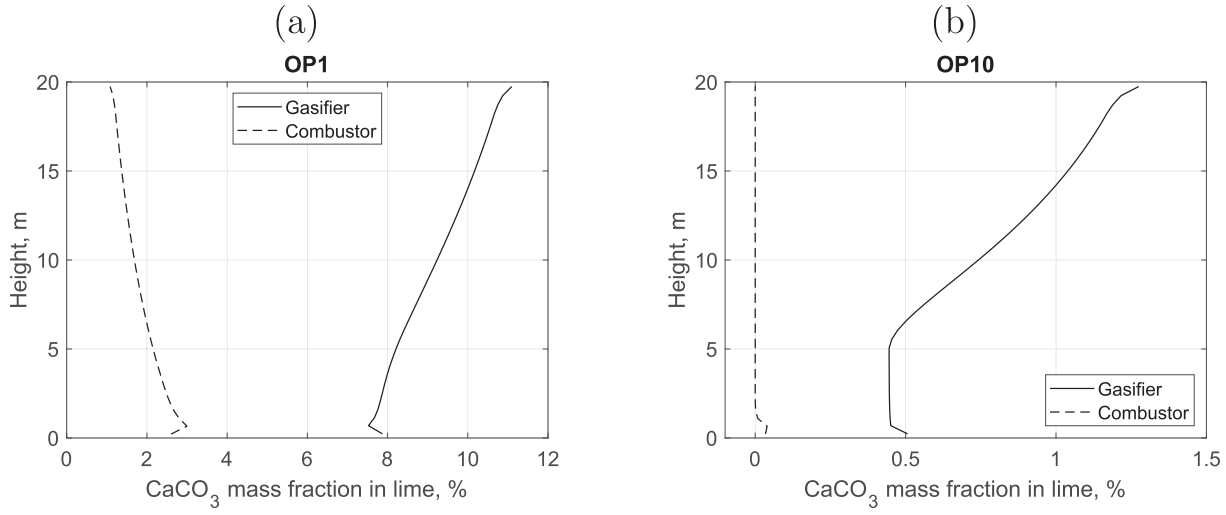

Fig. 14. Local $CaCO_3$ conversion degrees. (a) OP1 and (b) OP10.

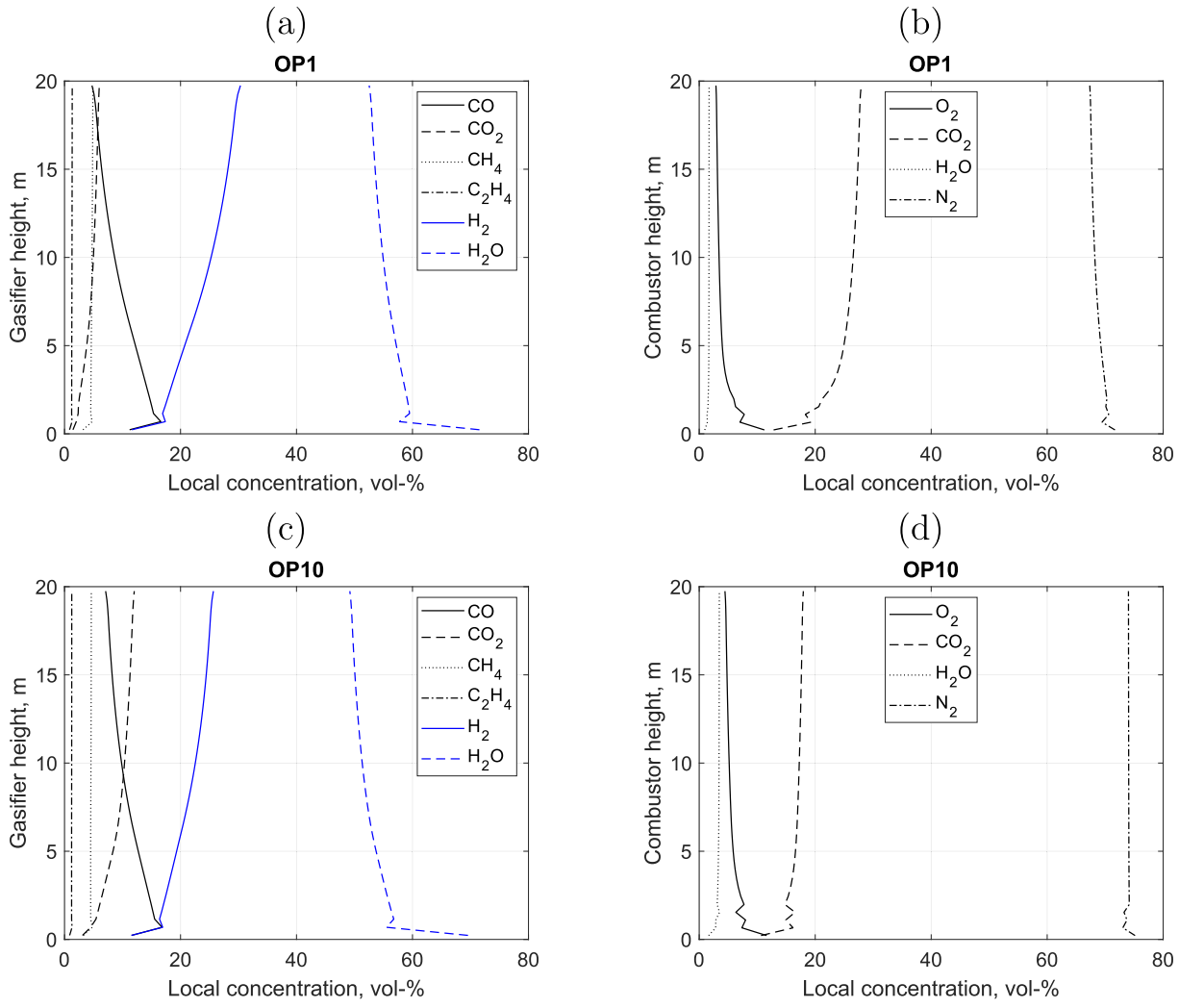

Fig. 15. Gas concentration profiles for both reactors at (a) OP1 and (b) OP10.

processes, it was found that the lime reactions and the water-gas shift reaction were the most significant reactions together with the decomposition of the fuel, which affect the yield and composition of the product gas. For lime reactions, an appropriate temperature level must be obtained for the carbonation in the gasifier in order to be able to control the CO_2 capture and water-gas shift reactions that ultimately determine the quality of the producer gas. A sufficiently high-temperature level must be reached on the combustor side so that the calcination is as efficient as possible, and the degree of lime material conversion will not limit the CO_2 capture in the gasifier. For the water-gas shift reaction, it is noted that the reaction does not reach equilibrium under SEG conditions, and this should be taken into account when using simplified reaction equilibrium modeling techniques. One important model development area is related to the hydrodynamics of the CFB reactor. For hydrodynamics, computational fluid dynamics can provide a good model development support. More accurate hydrodynamic submodels can provide a better prediction for intra- and inter-reactor flows, giving a more accurate model result for heat capacity flows. This also leads to a better and physically valid estimation for the operation of the whole process. The presented modeling method also provides an opportunity to study and compare different biomasses' suitability for the SEG process based on dual bed arrangement. However, this requires adequate preliminary data and physical sub-models for different biomasses' behavior under SEG conditions. The modeling method presented in this

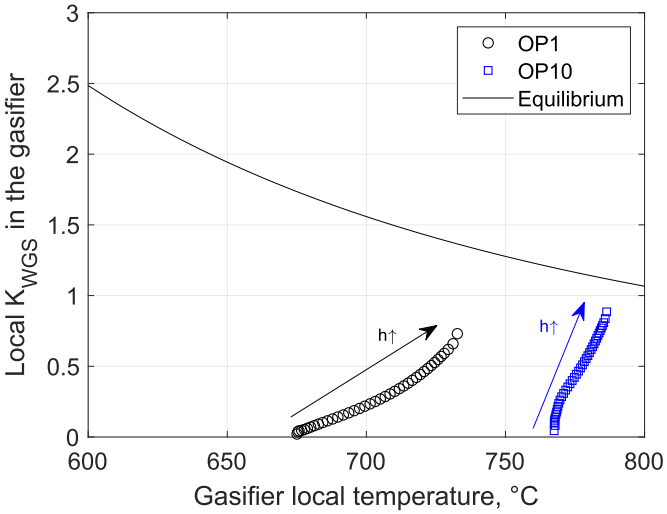

Fig. 16. Local water-gas shift reaction balance value in a function of local temperature. Arrows show the direction of the reactor's vertical axes.

work does not place constraints on the biomass under consideration, as long as it is possible to find and use sufficiently accurate descriptions of fuel decomposition at different temperatures, as well as main reaction descriptions. An industrial-scale plant's operating values presented in this work provide essential information to support plant design and assess plant operating performance and costs.

Author statement

Jouni Ritvanen: Conceptualization, Methodology, Software, Formal analysis, Visualization, Writing – original draft. Kari Myöhänen: Methodology, Writing – review & editing, Antti Pitkäoja: Visualization, Methodology, Writing – review & editing, Timo Hyppänen: Supervision, Writing – review & editing

Declaration of competing interest

The authors declare that they have no known competing financial interests or personal relationships that could have appeared to influence the work reported in this paper.

Acknowledgements

This work in FLEDGED project has received funding from the European Union's Horizon 2020 research and innovation programme under grant agreement No 727600.

Nomenclature

γ_i	Fuel decomposition model parameter, [−]
ρ	Density, [kg/m^3]
ρ_b	Bottom density, [kg/m^3]
ρ_e	Exit density, [kg/m^3]
A	Cross section area of the reactor, [m^2]
a, K	Decay parameters
C	Molar concentration, [mol/m^3]
E	Energy, [J]
f	Calibration factor, [−]
h	Height, [m]
i	Index, [−]
j	Index, [−]
k	Reaction rate factor, [1/s]
M	Module, $M = (y_{H_2} - y_{CO_2})/(y_{CO} + y_{CO_2})$
m	Mass, [kg]
M_i	Molar mass, [g/mol]
n_{tot}	Total number of 1D elements, [−]
P	Power, [W]
p	Pressure, [bar, atm, Pa]
$p\delta_{eq}$	Deviation from the reaction equilibrium, [−]
q_m	Mass flow rate, [kg/s]
q_r	Reaction heat, [W]
q_{adv}	Advection, [W]
q_{disp}	Energy dispersion, [W]
q_{ht}	Heat transfer, [W]
R	Universal gas constant, [J/(molK)]
R_i	Reaction rate, [kg/(m^{3}s)]
r_i	Reaction rate, [mol/(m^{3}s)]
$r_{j,i}$	Reaction rate, [kg/s]
T	Temperature, [K]
t	Time, [s]
T_{gasif}	Average gasifier temperature, [$^\circ$C]
u	Gas superficial velocity, [m/s]
u_t	Terminal velocity, [m/s]
u_{pn}	Transport velocity, [m/s]
W	Solid's mass fraction, [−]
x	Mass fraction, [−]
ar	As-received fuel
av	Average
BFB	Bubbling fluidized bed
boud	Boudouard reaction
calc	Calcination reaction
carb	Carbonation reaction
CC	Carbon conversion
CFB	Circulating fluidized bed
CGE	Cold gas efficiency
daf	Dry ash free fuel
db	Dry basis
desu	Desulphation reaction
dirs	Direct sulphation reaction
DME	Dimethyl ether
ds	Dry fuel
eq	Equilibrium
F	Fuel
LHV	Lower heating value, [MJ/kg]
mf	Methanation reaction
pg	Producer gas
S/C	Steam to carbon ratio, [mol/mol]
SEG	Sorption enhanced gasification
sulp	Sulphation reaction
vol	Volatile
wg	Water-gas reaction
wgs	Water-gas shift reaction

References

[1] European commission A. European strategy for low-Emission Mobility 2016. 2016.
[2] Pelkmans, L. European Union - 2018 update, Bioenergy policies and status of implementation. 2018.
[3] Corella J, Toledo JM, Molina G. A review on dual fluidized-bed biomass gasifiers. Ind Eng Chem Res 2007;46:6831–9. https://doi.org/10.1021/ie0705507.
[4] Pfeifer C. 22 - sorption-enhanced gasification. In: Scala F, editor. Fluidized bed technologies for near-zero emission combustion and gasification. Woodhead Publishing Series in Energy; Woodhead Publishing; 2013, ISBN 978-0-85709-541-1. p. 971–1001. https://doi.org/10.1533/9780857098801.4.971.
[5] Fuchs J, Schmid JC, Benedikt F, Müller S, Hofbauer H, Stocker H, Kieberger N, Bürgler T. The impact of bed material cycle rate on in-situ CO2 removal for sorption enhanced reforming of different fuel types. Energy 2018;162:35–44. https://doi.org/10.1016/j.energy.2018.07.199.
[6] Benedikt F, Schmid J, Fuchs J, Mauerhofer A, Müller S, Hofbauer H. Fuel flexible gasification with an advanced 100 kW dual fluidized bed steam gasification pilot plant. Energy 2018;164:329–43. https://doi.org/10.1016/j.energy.2018.08.146.
[7] Schweitzer D, Beirow M, Gredinger A, Armbrust N, Waizmann G, Dieter H, Scheffknecht G. Pilot-scale demonstration of oxy-SER steam gasification: production of syngas with pre-combustion CO2 capture. Energy Procedia 2016;86:56–68. https://doi.org/10.1016/j.egypro.2016.01.007.
[8] Fuchs J, Schmid JC, Müller S, Mauerhofer AM, Benedikt F, Hofbauer H. The impact of gasification temperature on the process characteristics of sorption enhanced reforming of biomass. Biomass Conversion and Biorefinery; 2019. https://doi.org/10.1007/s13399-019-00439-9.
[9] Hejazi B, Grace JR, Bi X, Mahecha-Botero A. Steam gasification of biomass coupled with lime-based CO2 capture in a dual fluidized bed reactor: a modeling study. Fuel 2014;117:1256–66. https://doi.org/10.1016/j.fuel.2013.07.083.
[10] Detchusananarda T, Ponpesha P, Saebeab D, Authayanunc S, Arpornwichanopa A. Modeling and analysis of sorption enhanced chemical looping biomass gasification. Chemical Engineering Transactions 2017;57:103–8. https://doi.org/10.3303/CET1757018.
[11] Beirow M, Parvez A, Schmid M, Scheffknecht G. A detailed one-dimensional hydrodynamic and kinetic model for sorption enhanced gasification. Appl Sci 2020;10(17). https://doi.org/10.3390/app10176136.
[12] Yan L, Cao Y, He B, Li X. Calcium looping enhanced biomass steam gasification in a two-stage fluidized bed gasifier. Energy Fuels 2018;32(8):8462–73. https://doi.org/10.1021/acs.energyfuels.8b01414.
[13] Hafner S, Schmid M. FLEDGED Deliverable D3.4 - Final experimental results on SEG process experiments at pilot (TRL5) scale for stationary and flexible operating regimes. 2020.
[14] Neves D, Thunman H, Matos A, Tarelho L, Gómez-Barea A. Characterization

and prediction of biomass pyrolysis products. Prog Energy Combust Sci 2011;37(5):611–30. https://doi.org/10.1016/j.pecs.2011.01.001.
[15] Myöhänen K. Modelling of combustion and sorbent reactions in three-dimensional flow environment of a circulating fluidized bed furnace. Ph.D. thesis; Lappeenranta University of Technology; 2011. http://urn.fi/URN:ISBN:978-952-265-161-7.
[16] Fang F, Li ZS, Cai NS. Experiment and modeling of CO2 capture from flue gases at high temperature in a fluidized bed reactor with Ca-based sorbents. Energy Fuels 2009;23(1):207–16. https://doi.org/10.1021/ef800474n.
[17] Martínez I, Grasa G, Murillo R, Arias B, Abanades JC. Kinetics of calcination of partially carbonated particles in a Ca-looping system for CO2 capture. Energy Fuels 2012;26(2):1432–40. https://doi.org/10.1021/ef201525k.
[18] Silcox GD, Kramlich JC, Pershing DW. A mathematical model for the flash calcination of dispersed calcium carbonate and calcium hydroxide particles. Ind Eng Chem Res 1989;28(2):155–60. https://doi.org/10.1021/ie00086a005.
[19] Grasa G, Murillo R, Alonso M, Abanades JC. Application of the random pore model to the carbonation cyclic reaction. AIChE J 2009;55(5):1246–55. https://doi.org/10.1002/aic.11746.
[20] Rajan RR, Wen CY. A comprehensive model for fluidized bed coal combustors. AIChE J 1980;26(4):642–55. https://doi.org/10.1002/aic.690260416.
[21] Risnes H, Sorensen L, Hustad J. CO2 reactivity of chars from wheat, spruce and coal. In: Bridgewater A, editor. Progress in thermochemical biomass conversion. Oxford: Blackwell Science; 2001. p. 61–72.
[22] Hemati M, Laguerie C. Determination of the kinetics of the sawdust steam-gasification of charcoal in a thermobalance. Entropie 1988;142:29–40.
[23] Hejazi B, Grace J, Bi X, Mahecha-Botero A. Kinetic model of steam gasification of biomass in a bubbling fluidized bed reactor. Energy Fuels 2017;31(2):1702–11. https://doi.org/10.1021/acs.energyfuels.6b03161.
[24] Biba V, Macák J, Klose E, Malecha J. Mathematical model for the gasification of coal under pressure. Ind Eng Chem Process Des Dev 1978;17(1):92–8. https://doi.org/10.1021/i260065a017.
[25] Basu P. Combustion and gasification in fluidized beds. CRC Press; 2006.
[26] Ansys® Fluent. Release 2020;19.2.
[27] Adánez J, Miranda J, Gavilán J. Kinetics of a lignite-char gasification by CO2. Fuel 1985;64(6):801–4. https://doi.org/10.1016/0016-2361(85)90013-4.
[28] Oguma A, Yamada N, Furusawa T, Kunii D. Preprint for the 11th fall meeting of the soc. Of chem. Eng. Japan 1977:121.
[29] Sergeant GD, Smith IW. Combustion rate of bituminous coal char in the temperature range 800 to 1700 K. Fuel 1973;52(1):52–7. https://doi.org/10.1016/0016-2361(73)90012-4.
[30] Gibson M, Euker C. Mathematical modelling of fluidized bed coal gasification. In: AIChE meeting; 1975.
[31] Johnson J. Kinetics of coal gasification. New York: John Wiley; 1979.
[32] Johnsson F, Leckner B. Vertical distribution of solids in a CFB-furnace. In: Proceedings of the 13th international conference on fluidized bed combustion. Orlando, USA: ASME; 1995. p. 671–9.
[33] Ylätalo J. Model based analysis of the post-combustion calcium looping process for carbon dioxide capture. Ph.D. thesis. Lappeenranta University of Technology; 2013. http://urn.fi/URN:ISBN:978-952-265-521-9.